Received: 13 December 2022 | Revised: 7 March 2023 | Accepted: 15 March 2023

DOI: 10.1002/mrm.29654

RESEARCH ARTICLE

Magnetic Resonance in Medicine

Electromagnetic and RF pulse design simulation based optimization of an eight-channel loop array for 11.7T brain imaging

Son Chu[1] | **Vincent Gras**[2] | **Franck Mauconduit**[2] | **Aurélien Massire**[3] | **Nicolas Boulant**[2] | **Shajan Gunamony**[1]

[1]Imaging Centre of Excellence, University of Glasgow, Glasgow, UK

[2]University of Paris-Saclay, CEA, CNRS, BAOBAB, NeuroSpin, Gif sur Yvette, France

[3] Siemens Healthcare SAS, Saint-Denis, France

Correspondence
Shajan Gunamony, Imaging Centre of Excellence, University of Glasgow, Glasgow, G51 4LB, UK.
Email: shajan.gunamony@glasgow.ac.uk

Funding information
Horizon 2020 Framework Programme, Grant/Award Number: 885876; Agence Nationale de la Recherche, Grant/Award Number: ANR-21-ESRE-0006

Purpose: Optimization of transmit array performance is crucial in ultra-high-field MRI scanners such as 11.7T because of the increased RF losses and RF nonuniformity. This work presents a new workflow to investigate and minimize RF coil losses, and to choose the optimum coil configuration for imaging.

Methods: An 8-channel transceiver loop-array was simulated to analyze its loss mechanism at 499.415 MHz. A folded-end RF shield was developed to limit radiation loss and improve the B_1^+ efficiency. The coil element length, and the shield diameter and length were further optimized using electromagnetic (EM) simulations. The generated EM fields were used to perform RF pulse design (RFPD) simulations under realistic constraints. The chosen coil design was constructed to demonstrate performance equivalence in bench and scanner measurements.

Results: The use of conventional RF shields at 11.7T resulted in significantly high radiation losses of 18.4%. Folding the ends of the RF shield combined with optimizing the shield diameter and length increased the absorbed power in biological tissue and reduced the radiation loss to 2.4%. The peak B_1^+ of the optimal array was 42% more than the reference array. Phantom measurements validated the numerical simulations with a close match of within 4% of the predicted B_1^+.

Conclusion: A workflow that combines EM and RFPD simulations to numerically optimize transmit arrays was developed. Results have been validated using phantom measurements. Our findings demonstrate the need for optimizing the RF shield in conjunction with array element design to achieve efficient excitation at 11.7T.

KEYWORDS

11.7T MRI, parallel transmit, transmit array design, UHF MRI

1 | INTRODUCTION

The MRI community has been continuously pushing for higher static magnetic fields with an aim to image the cortical layers and columnar structures at sub-millimeter scale. The promise of a supra-linear boost in SNR, which enables higher resolution imaging as well as unique imaging contrasts, is driving the development of MRI at ultra-high field (UHF) strengths, such as 7T and beyond.[1–8] Because of the advances in hardware and MRI methods development, 7T scanners have achieved regulatory approval as a medical device for limited applications.[9,10] To date, stronger magnets such as 9.4T and 10.5T are being used in neuroscience and clinical research.[11–13] Following the trend in increasing static magnetic field strength, a whole-body 11.7T scanner is now operational at CEA, Neurospin, Saclay.[14–16] Further 10.5T and 11.7T scanners are being planned[17] and even a 14T human MRI scanner is currently under consideration.[18]

However, there are significant challenges associated with UHF MRI such as inhomogeneous B_1^+ field, increased RF power deposition,[1,4] and an increase in magnetic susceptibility and other imaging artifacts.[1,4,6,19] Because of the increase in magnetic field strength, the Larmor frequency increases due to the increase in magnetic field strength and the RF wavelength in tissue becomes shorter than the dimension of the object to be imaged.[20] Especially at 11.7T, the corresponding wavelength in average brain tissue is ~7 cm, which is approximately one-third of the largest dimension of the human head.

The RF power applied to the transmit coil deposits energy in the biological tissue, and this increases with field strength.[4] Due to the short wavelength, the interactions between the tissue and the electromagnetic (EM) field results in a spatially dependent energy deposition, which increases the potential for localized RF heating.[21] The energy deposition during routine exams is controlled by the specific absorption rate (SAR) limits, which is a measure of the RF power absorbed per unit mass. Therefore, the ability to provide an efficient and homogeneous RF excitation while operating within the SAR constraints is one of the most important engineering requirements in designing RF transmit coils for UHF MRI.

Transmit arrays are a well-established tool in mitigating the B_1^+ field inhomogeneities at UHF because they offer additional degrees of freedom to manipulate the amplitude and phase of the currents fed to each individual coil element.[22–27] The performance of transmit arrays is often assessed in terms of transmit efficiency ($B_1^+/\sqrt{P}$), safety excitation efficiency ($B_{1\mathrm{avg}}^+/\sqrt{\mathrm{SAR}_{10\,\mathrm{g\,(max)}}}$), and coupling between the coil elements.[22–24] Because of the high operating frequency at 11.7T (499.415 MHz), the Ohmic losses in discrete components are significantly higher in addition to the losses in biological tissue. Practical considerations include the cable loss between the coil input and the RF power amplifier, which can be as high as 3 dB or even more, and limited output power levels from the amplifiers.

In addition, coil configuration also plays an important role in designing transmit arrays. Typically, transmit arrays can be categorized into two groups, namely transceiver arrays[25,27] and transmit-only receive-only arrays.[22,24,28] The latter is used most, especially for imaging the brain, because the number of receive channels is not limited by the number of transmit channels. High-density receive arrays have been shown to be beneficial particularly because of their enhanced parallel imaging performance at UHF.[29,30] However, to accommodate the receive array, the transmit array in transmit-only receive-only configuration must be constructed on a larger coil housing (typical dimensions for head coils range from 280 to 300 mm diameter tubes), which can further reduce transmit efficiency because the transmit elements are further away from the sample.

Therefore, optimizing the array design and extracting every performance out of the transmit array is an essential requirement for UHF MRI. In this work, we have developed a proof-of-concept 8-channel transceiver array for imaging at 11.7T. The design optimization workflow combines 3D EM and RF pulse design (RFPD) simulations to achieve efficient excitation within SAR constraints. The design process involved extensive numerical simulations to analyze and minimize various loss mechanisms, optimizing the coil design in conjunction with the RF shield design, and using the EM fields in RFPD simulations to select the optimal array. The chosen array has been constructed and phantom results as well as ex vivo brain images are presented in this article. In this proof-of-concept work, an 8-channel transmit array was considered and the dimensions of the RF shield as well as the coil length were varied. Future work will involve 16-channel dual-row designs as they have been shown to enhance parallel transmit performance at UHF.[31]

2 | METHODS

2.1 | Optimization workflow

In this work, we adopted a new workflow for designing transmit arrays, which combines EM simulations along with RFPD simulations. First, a detailed numerical model of the coil was created in the EM simulation tool, CST Studio Suite 2021 (Dassault Systems). To identify all sources of losses within the array, the power budget was investigated. The next step included optimizing the coil design to minimize RF losses and hence, increase the power delivered

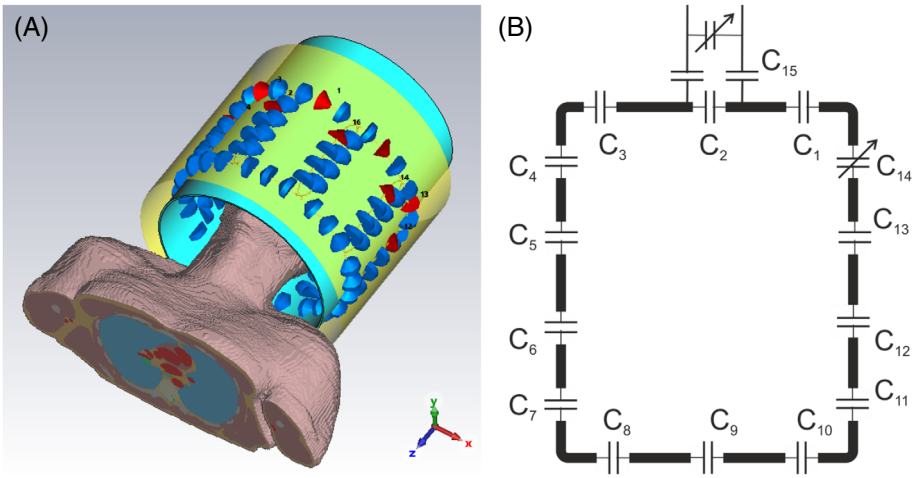

FIGURE 1 (A) Numerical model of the transmit array with a cylindrical shield. The lumped elements (capacitors, blue), the simulation ports (red), and the Duke body model, which was truncated to the level of shoulders are shown. (B) Equivalent circuit of a single transmit element.

to the biological tissue. This could result in different coil configurations exhibiting similar transmit efficiency. To determine the optimal array for imaging, the workflow included RFPD simulations, which were performed under realistic SAR and power constraints and consisted of safety factors for the predictions to be close to the use-case scenario. The chosen array was then constructed, and the simulation results were validated using phantom scans.

2.2 | Coil model

A detailed model of the transmit array was created in CST, and simulations were performed using its time-domain solver, which uses finite-integration techniques together with RF circuit co-simulation.[32,33] The coil design consisted of eight identical rectangular loops arranged on a fiberglass tube with 285-mm inner diameter ($\varepsilon_r = 5.5$, $\tan\delta = 0.04$, wall thickness = 2.5 mm). This diameter was chosen to allow space for a receive-only array. In the numerical domain, the loops were made of 2-mm perfect electric conductor wires. Each loop was segmented to accommodate a total of 14 evenly distributed capacitors (13 fixed capacitors and one trimmer) to tune the loops to 499.415 MHz, which corresponds to a segment length of $\lambda/15$. This was empirically determined to ensure that the coil tuning is not dominated by the capacitive coupling to the sample.[34] The array elements were matched to 50 Ω through a balanced matching circuit.[35] The equivalent circuit is shown in Figure 1A. The fixed capacitors were represented by lumped elements (blue), whereas the matching circuit and variable capacitors were substituted by 50-Ω discrete ports (red), as shown in Figure 1B. Fixed capacitors were modeled with an equivalent series resistance of 0.438 Ω and an equivalent series inductance of 1.24 nH, which corresponds to 2.4 pF 100C-series capacitors (American Technical Ceramics) at 500 MHz. Although 100C-series capacitors were chosen because of component availability, it is possible to further reduce the Ohmic loss by selecting lower loss component, for example 800C-series. The variable capacitors (two per channel) were simulated as ideal capacitors. The transmit array elements were tuned and matched to the Duke body model from the virtual family,[36] which had a 2-mm isotropic resolution and was truncated below the shoulder level. Variable capacitors for tuning and matching were adjusted in circuit co-simulations to achieve an impedance match of better than −40 dB for each channel.

The array was decoupled by geometrically overlapping adjacent elements until minimum transmission coefficient (S_{21}) value was reached. The scanner bore was represented by a copper RF shield of 640-mm diameter and 1500 mm in length. The initial model also consisted of a 300-mm long cylindrical RF shield with a diameter of 350 mm. All losses between the coil input and the scanner coil plug such as cable loss and TR switch loss were measured at 499.415 MHz and modeled as an attenuator in circuit co-simulation. Individual B_1^+ field maps were combined using the linearity superposition principle. To obtain the circularly polarized (CP) mode, an equal power of 1 Watt (W) was applied to all channels with an incremental phase offset of 45°. The power budget and B_1^+ field maps were then obtained using post-processing options available in CST for CP mode excitation.

To ensure that all ports and lumped elements were connected properly, local mesh refinement with a step width of 0.7 mm in all directions was set for the electric conductors. All simulations used broadband excitations from 440 MHz to 540 MHz with perfectly matched layers placed at a distance of one-fourth of the wavelength at 499.415 MHz. The accuracy of numerical simulations was secured by setting a convergence criterion of −40 dB for the amplitude of the port signals at the end of the simulation time interval. A typical simulation consisted of ~55 million mesh cells and took ~12 h on a customized Z8 G4 HP workstation equipped with a dual Xeon Gold 5222

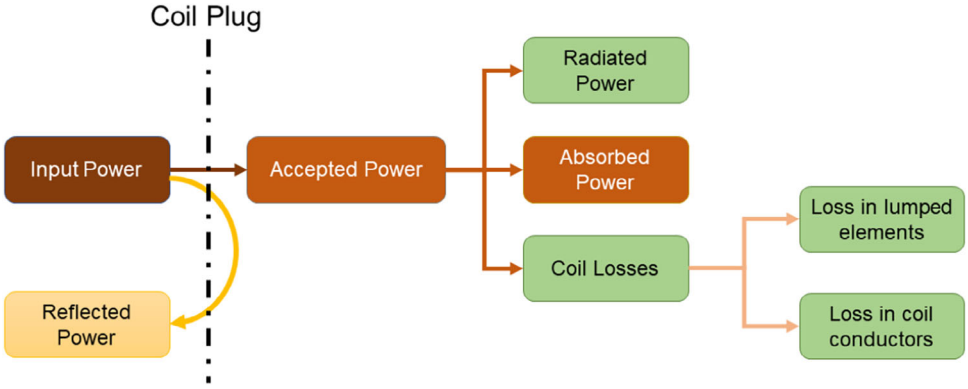

FIGURE 2 The power budget identifies all sources of losses to the power applied to the coil. This information can be used to implement methods to minimize controllable losses such as reflected power, radiated power, and coil component losses.

processor, 96GB RAM, and one NVidia Quadro RTX 5000 GPU acceleration card.

2.3 | Power budget analysis

The power budget analysis was conducted to identify all the loss mechanisms within the transmit array.[34,37] This offers insights into the sources of losses and implements methods to minimize controllable losses. A snapshot of the loss mechanisms is shown in Figure 2. The input power is the total incident power at the coil plug and the reflected power represents power lost because of impedance mismatch and inter-element coupling. Reducing the coupling and achieving a good impedance match ensures that the accepted power in the coil structure is close to the input power. The power accepted in the coil structure can be subdivided into power lost because of radiation, coil component losses, and power absorbed in the biological tissue.

The optimal design of a transmit array should involve identifying all loss mechanisms to optimally use the available RF power in the scanner and achieve efficient transmit excitation within the SAR constraints. Although coil losses caused by the intrinsic resistances in the lumped elements and conductors can be easily minimized by carefully selecting low-loss components and materials, engineering challenges still remain for reducing the reflected power and radiated power, especially at 11.7T.

2.4 | Minimization of RF losses using electromagnetic simulation

The reference design included a conventional cylindrical RF shield (350-mm diameter, 300-mm length) similar to the ones used in 7T coils to reduce radiation loss.[38] Although this array could be welldecoupled and very low reflected power could be achieved, a significant amount of the input power was radiated in the scanner bore, thereby resulting in a weak B_1^+ field distribution in the head model. This loss in performance is because of the cutoff frequency of the conventional cylindrical shield, which is ~502 MHz in free-space and very close to the Larmor frequency of hydrogen nuclei (499.415 MHz) at 11.7T, and this supports wave propagation. To prevent this radiation loss and hence, improve the power absorbed in the sample at 11.7T, the cutoff frequency of the local RF shield must be increased. Several techniques such as dielectric and metallic loading have been reported in the literature to alter the dispersion characteristic of a circular waveguide.[39] Dielectric lining could be expensive, and it can increase the overall weight of the coil. Hence, the simplest form of metallic loading in which the ends of the cylindrical shield were folded until the inner tube was implemented. We found that the folded-end shield was sufficient to minimize the radiation loss. Furthermore, the implementation of the folded-end shield has no adverse effect on the coil usability and its openness because the folded sections of the RF shield extend from the outer tube to the inner tube of the array.

All subsequent optimizations of the transmit array design were conducted with the folded-end shield in place. However, designing coils for human brain MRI at 11.7T is unprecedented and parameters such as optimum shield diameter and shield length are yet unknown. The extent of the loop along the z-direction, the diameter of the RF shield, and the distance from the ends of the loop to the folded-end sections were varied to determine the configuration that offered the best transmit performance. For each configuration, the adjacent element overlap had to be individually adjusted to achieve robust S-parameter performance and minimize the reflected power. This is time-consuming and laborious because full 3D EM simulations had to be performed for every change in geometry.

To keep the number of simulations tractable, three loop lengths were chosen: 12 cm (array-α), 15 cm (array-β), and 16 cm (array-γ). The diameter of the RF shield was varied from 400 to 450 mm. A snapshot of the different coil models is shown in Figure 3. In each case, the loops were always placed at an equal distance from the folded-end

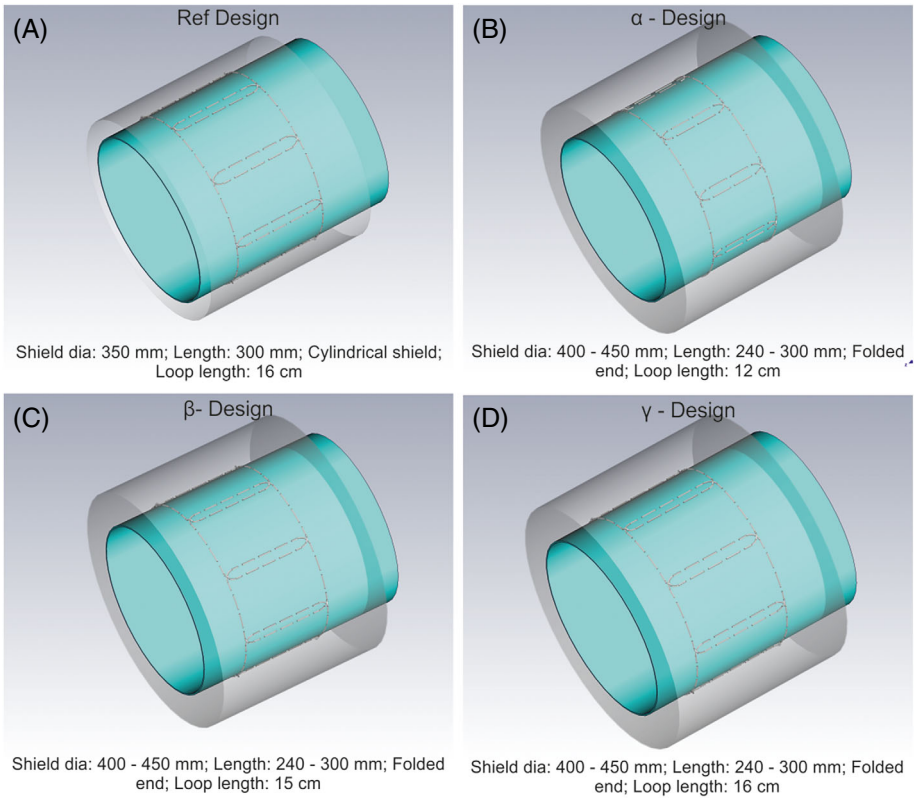

FIGURE 3 A snapshot of the different coil configurations considered in the electromagnetic and RF pulse design simulations is shown. The reference design consisted of a conventional RF shield similar to the ones used in 7T head coils.

sections. The length of the RF shield was varied from 240 to 300 mm with 20-mm increments. Altering the shield length in effect corresponds to optimizing the distance between the loops and the folded end of the shield. In addition to power budget analysis, the transmit efficiency and coverage of all configurations were compared in CP mode. Each version can be identified as follows: for example, $\alpha_{450}(280)$ represents an array with 12-cm loops, 450-mm shield diameter, and 280-mm shield length. The total number of EM simulations given all the configurations above was 24 ($3 \times 2 \times 4$).

2.5 | Array selection using radiofrequency pulse design simulations

To select the optimal array for imaging, the design optimization included RFPD simulations. The simulated electric and magnetic field maps from CST were exported on a 5-mm isotropic grid. Given the B_1^+ maps, RFPD simulations consisted of homogenizing the flip angle on a brain mask. The RFPD simulations were performed under the following settings to mimic realistic scenarios and constraints: 0.92 dB attenuation factor in power on field maps for cable losses, 1.5 safety factor for inter-subject variability in virtual observation points;[40,41] peak 10-g SAR (10 W/kg), global SAR (3.2 W/kg), maximum voltage per channel (220 V), average power per channel (6 W); brain mask; 5 and 7 k_T-points[42] for small tip angle (10°), and inversion (180°) pulses, respectively; active-set algorithm/transmit k-space trajectory optimization;[43,44] 40 initial random seeds; and 300 iterations.

The inversion pulse was 4-ms long. Durations of 0.5 ms (short) and 1 ms (long) were attempted for the small tip angle pulse to see the potential impact of SAR and power constraints. For the calculation of the constraints, a TR of 15 ms was considered for the small tip angle pulses (3D GRE sequence). For the inversion pulse, a TR of 3 s (MPRAGE) was taken into account. The flip angle normalized root mean square error (NRMSE) results were compared to select the optimal configuration for imaging.

2.6 | Proof-of-concept coil

The best-performing coil configuration was chosen and constructed as an 8-channel transceiver array with built-in TR switches (Figure 4A). The array consisted of two concentric fiberglass tubes with inner diameters of 285 mm and 400 mm, respectively. There were three rings that connect the two tubes together and stabilize the whole assembly. The folded sections of the RF shield were realized on the inner faces of the lower ring and the middle ring as shown in Figure 4A,B. The main cylindrical shield was slotted to reduce eddy currents and realized using double-sided flexible PCB (PW Circuits). It was glued onto

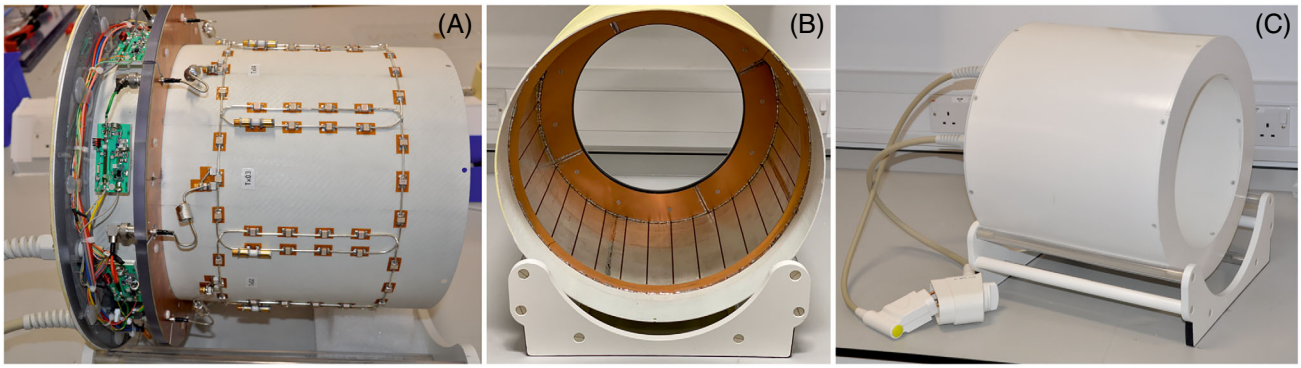

FIGURE 4 (A) Photograph of the internal hardware with coil elements, cable traps, and built-in TR switches, (B) implementation of the folded-end RF shield, and (C) fully assembled transceiver array.

the inner surface of the outer tube (Figure 4B). A picture of the completed coil is shown in Figure 4C.

The equivalent circuit of a single element of the constructed coil is as per the schematic shown in Figure 1A. A shielded solenoid cable trap tuned to 499.415 MHz was connected between the coil input and the TR switch. Solder pads were attached to the surface of the fiberglass tube to solder the components. Each transmit element consisted of evenly distributed fixed capacitors (13×, 2.4 pF, 100C-series; American Technical Ceramics) and a trimmer capacitor (1–7.5 pF, 5610-series; Johanson Manufacturing Corporation). The capacitors were interconnected using 2-mm diameter silver-plated copper wire (APX, France). All bench measurements were carried out by loading the coil with a head and shoulder phantom filled with tissue equivalent solution ($\varepsilon_r = 48.7$ and $\sigma = 0.65$ S/m at 500 MHz). The insertion loss of the custom-built TR switches and the 8-channel parallel transmit cable between the coil input and the coil plug was measured, and this attenuation was then incorporated in CST circuit co-simulation.

2.7 | Phantom and ex vivo brain measurement

B_1^+ mapping measurements were performed at 11.7T using the head and shoulder phantom and the selected RF coil configuration. The sequence used was the actual flip angle imaging[45] implemented in interferometric mode.[46] Parameters were TR = 240 ms, 3.2-mm isotropic resolution, and TA = 10 min 48 s per channel. Measured complex B_1^+ maps were compared with the EM simulations after additional scaling for unaccounted losses.

Finally, for additional demonstration and proof of concept, an RF pulse design was performed based on measured B_1^+ maps and parametrized with 6 k_T-points (total pulse duration of 0.5 ms) acquired on an ex vivo human brain with a target flip angle of 5°. The RF pulse solution was inserted in a 3D GRE sequence (TR = 30 ms, 0.85-mm isotropic resolution, TE = 2.6 ms, sagittal orientation, iPAT = 2, bandwidth per pixel = 770 Hz, and TA = 12 min 24 s).

3 | RESULTS

3.1 | Effect of folded-end shield

For the reference design with a conventional cylindrical RF shield, the average decoupling between the adjacent array elements and the next-neighboring elements were −23 dB and −18 dB, respectively, with a maximum coupling of −17 dB. As a result, the reflected power was minimal (1%). However, only 44% of the input power was delivered to the biological tissue and a significant amount of power (18.4%) was radiated from the system (Figure 5A). This results in a weak B_1^+ field across the sample with the maximum value of 1.04 μT for 8-W input power (Figure 5B), and the energy lost because of wave propagation along the scanner bore can be seen in Figure 5C. The effect of folding the ends of the RF shield can be seen on the power budget shown in Figure 5A and on the snapshot of the decreased wave propagation along the scanner bore in Figure 5D. The radiated power was reduced to 9.2% of the input power and the field was confined within the RF shield, resulting in a stronger B_1^+ field across the sample. Note that on all the power budget plots presented in this paper, the 1.25 dB attenuation factor that was added to represent the cable and TR switch loss until the coil plug should be considered for all the power terms to be conserved.

These initial results demonstrate that folding the ends of the RF shield is already effective in reducing the radiation loss. However, it also shows that the array performance can be improved further by minimizing the controllable losses. The next sections present the results of

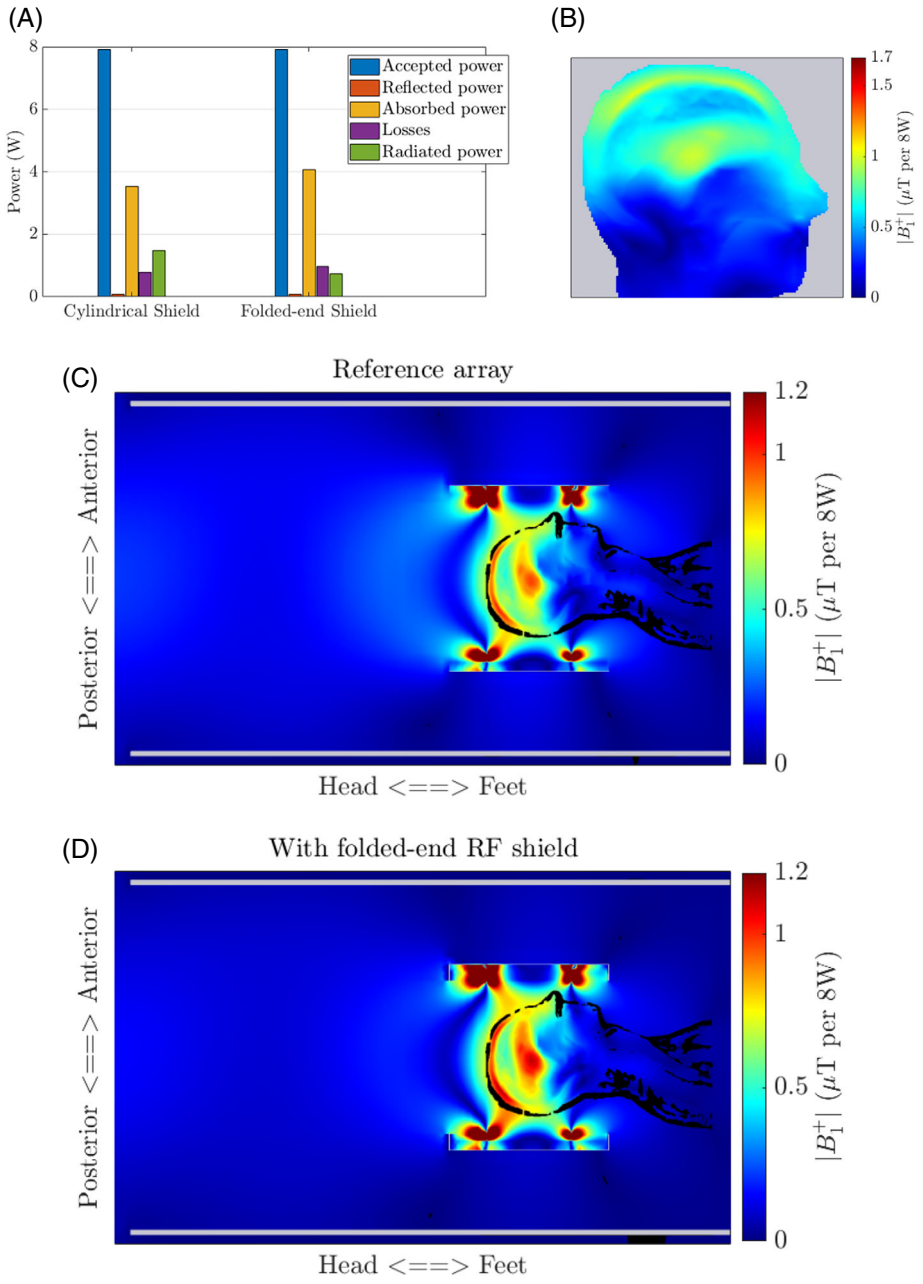

FIGURE 5 (A) Power budget comparison between the reference array with a cylindrical RF shield and that with a folded-end RF shield before optimization of the RF shield dimensions. (B) Sagittal slice of B_1^+ field map of the reference array in the Duke model. The peak B_1^+ field in the center of the brain is ~1.04 μT for 8-W input power in circularly polarized mode. (C) Demonstration of wave propagation in the scanner bore. (D) Reduced wave propagation because of the folded-end RF shield and higher B_1^+ in the sample.

the transmit array optimization in conjunction with the RF shield design to achieve efficient transmit excitation.

3.2 | Coil length and shield diameter

For the results shown in this section, the length of the RF shield is kept constant at 300 mm. Power budget analysis of four configurations consisting of 12- and 16-cm long loop elements and shield diameters of 400 and 450 mm are shown in Figure 6A. These are denoted as $\alpha_{400}(300)$, $\alpha_{450}(300)$, $\gamma_{400}(300)$, and $\gamma_{450}(300)$. Optimizing the coil in conjunction with the shield reduced the radiated power to ~9%, 4%, 5%, and 1% for these four arrays, respectively. As seen in Figure 6A, the power absorbed in the tissue increases as the losses are minimized. This would result in improved sample loading and a higher B_1^+ compared to the reference array. Note that the results of β-arrays are not included for simplicity. Furthermore, its performance was found to be in between the α-arrays and γ-arrays.

Histograms of the magnitude of the B_1^+ field generated by these arrays in CP mode are shown in Figure 6B. The α-configurations exhibited larger lower tails in the histogram, representing a more inhomogeneous B_1^+ distribution. This is mainly because of the 12-cm array offering less coverage along the z-direction compared to the 16-cm array. The coefficients of variation (CV) defined as the

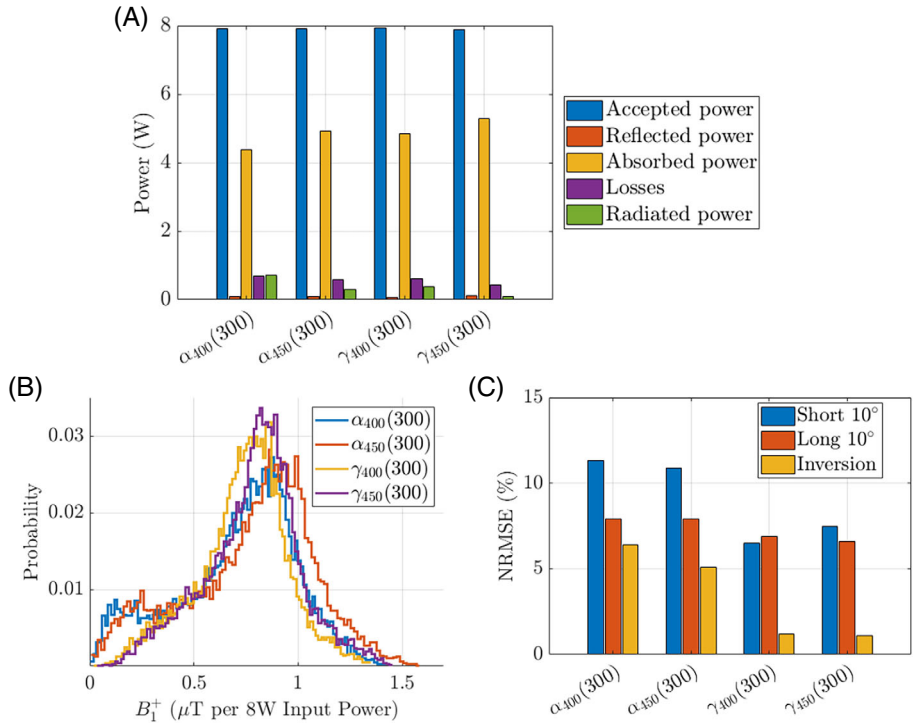

FIGURE 6 Simulated (A) power budget and (B) histograms of the magnitude of the B_1^+ fields for 8 W input power (circularly polarized mode) in the brain tissues for different α and γ designs with the same shield length of 300 mm. (C) NRMSEs in percent for three different RF pulse design simulations: short duration 10°, long duration 10°, and inversion pulse.

standard deviation over the mean, which is a measure of the B_1^+ homogeneity in CP mode, were calculated as follows:

$$\mathrm{CV}\,[\alpha_{400}(300)] = 41\%, \mathrm{CV}\,[\alpha_{450}(300)] = 39\%,$$
$$\mathrm{CV}\,[\gamma_{400}(300)] = 27.1\%, \text{and } \mathrm{CV}\,[\gamma_{450}(300)] = 27.4\%.$$

The CV of α-arrays in CP mode therefore was significantly higher compared to the γ-designs.

The α-designs achieved higher peak B_1^+ in the center of the brain compared to the γ-designs because they excited a smaller volume while using the same input power. The values were 1.55 and 1.7 μT versus 1.48 and 1.58 μT for 8-W input power. Moreover, it is worth noting that for all array configurations the larger shield (shield 2) provided less radiated power, fewer losses in lumped components and metallic parts, and more absorbed power in the sample. Therefore, for both designs, the peak B_1^+ was higher for the larger 450-mm folded-end RF shield.

Ultimately, from the RFPD simulations, α-configurations exhibited larger flip angle NRMSEs of the k_T-points for all three different pulses as shown in Figure 6C. As a result, the γ-configurations were chosen for further optimization.

3.3 | Length of RF shield

The final step in the optimization process was to investigate the influence of the distance between the folded ends of the RF shield and the loop conductors. Figure 7A,B show the power budget of arrays γ_{400} and γ_{450} with shield length from 240 to 300 mm. The radiated power was <5% for all arrays. Furthermore, the radiation loss was minimum for the 240-mm length shield in the case of γ_{400} and the 300-mm shield length for γ_{450}. The reduction in radiation loss consequently increased the absorbed power (Figure 7A,B).

Figure 7C,D is histograms of the magnitude of CP-like B_1^+ fields inside the brain for all γ-designs. The coefficients of variation are very similar:

$$\mathrm{CV}\,[\gamma_{400}(240)] = 26.7\%, \mathrm{CV}\,[\gamma_{400}(260)] = 26.7\%,$$
$$\mathrm{CV}\,[\gamma_{400}(280)] = 27.0\%, \mathrm{CV}\,[\gamma_{400}(300)] = 27.1\%,$$
$$\mathrm{CV}\,[\gamma_{450}(240)] = 27.1\%, \mathrm{CV}\,[\gamma_{450}(260)] = 27.4\%,$$
$$\mathrm{CV}\,[\gamma_{450}(280)] = 27.4\%, \text{and } \mathrm{CV}\,[\gamma_{450}(300)] = 27.4\%.$$

To choose the most suitable array for imaging, the RFPD simulations were carried out once again. NRMSEs of the k_T-point pulses are shown in Figure 7E.

From an RF engineering point of view, the best EM performances correspond to γ_{400} (240) and γ_{450}(280) because they had the least radiated power as well as the most power absorbed in the head. However, based on the results of the RFPD simulations, both designs γ_{400}(260) and γ_{450}(240) are superior in terms of imaging as their simulated flip angle maps were slightly more homogeneous. Although these two arrays could provide similar transmit performance, γ_{400}(260) was chosen for construction because of the smaller shield diameter. A larger RF shield would

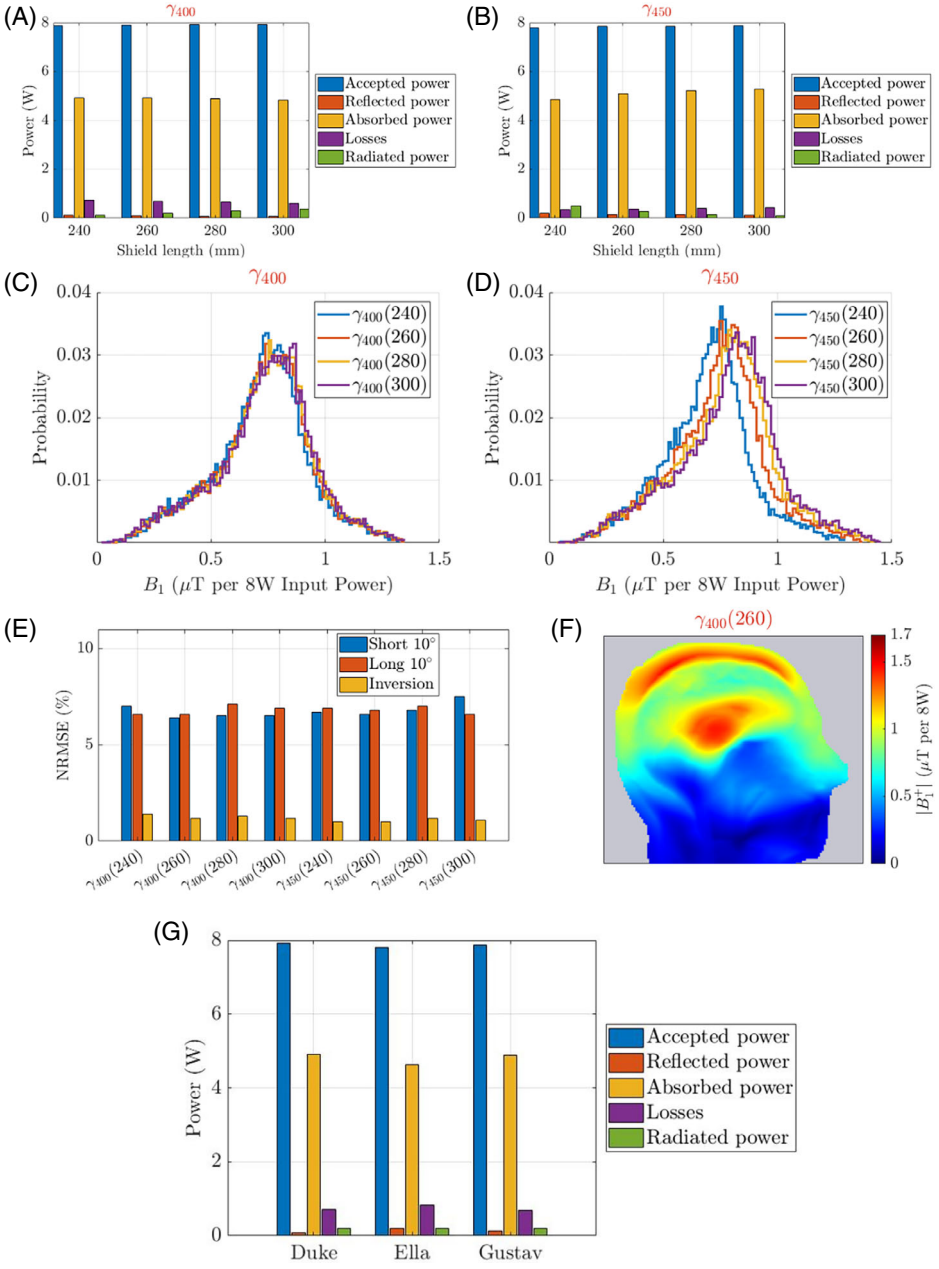

FIGURE 7 (A,B) Power budget and (C,D) histograms of the magnitude of the B_1^+ fields for 8-W input power for γ_{400} and γ_{450} designs with four shield lengths: 240, 260, 280, and 300 mm. (E) NRMSEs in percent for three different RF pulse design simulations: short 10°, long 10°, and inversion pulse. (F) Sagittal slice of B_1^+ field map of $\gamma_{400}(260)$. The peak B_1^+ in the center of the brain while driving the coil in CP mode is 1.48 μT for 8-W input power. (G) Simulated power budget of the chosen array with three body models demonstrates the robustness of the design.

offset the coil from the isocenter when placed on the patient table. In comparison to the reference array, the design optimization steps resulted in an improvement of 42.3% in the simulated peak B_1^+ field in the center of the brain (from 1.04 to 1.48 μT) with $\gamma_{400}(260)$ (Figure 7F). Additionally, the loss in the discrete components as well as the loss in metal of the chosen array reduced from 9.8% to 8.6%. Two more body models were simulated to verify the robustness of the chosen design (Figure 7G). Furthermore, the CV of the chosen array reduced from 33% to 26.7%.

3.4 | Coil validation

Figure 8A,B demonstrates good agreement between the simulated and measured S-parameters of array $\gamma_{400}(260)$ when loaded with a head and shoulder phantom. All channels were matched to better than −30 dB in both simulation and measurement. A higher level of decoupling was achieved in the constructed coil because the overlap between the neighbor elements was adjusted individually while all overlaps were of the same distance in the simulations. The average adjacent and next-neighbor coupling are −20.5 dB and −16.5 dB in the simulation versus −26.7 dB and −15.6 dB in the experiment, respectively.

Figure 9 compares the simulated and experimental B_1^+ field maps in the tissue-equivalent phantom while driving the coil in CP mode. Overall, there is good agreement in the spatial distribution of the B_1^+ field between simulation and measurement. Furthermore, the simulated peak B_1^+ in the center of the phantom's head was 1.90 μT per 8-W input power at the coil plug, whereas the measured value was 1.85 μT. Discrepancies between the simulations

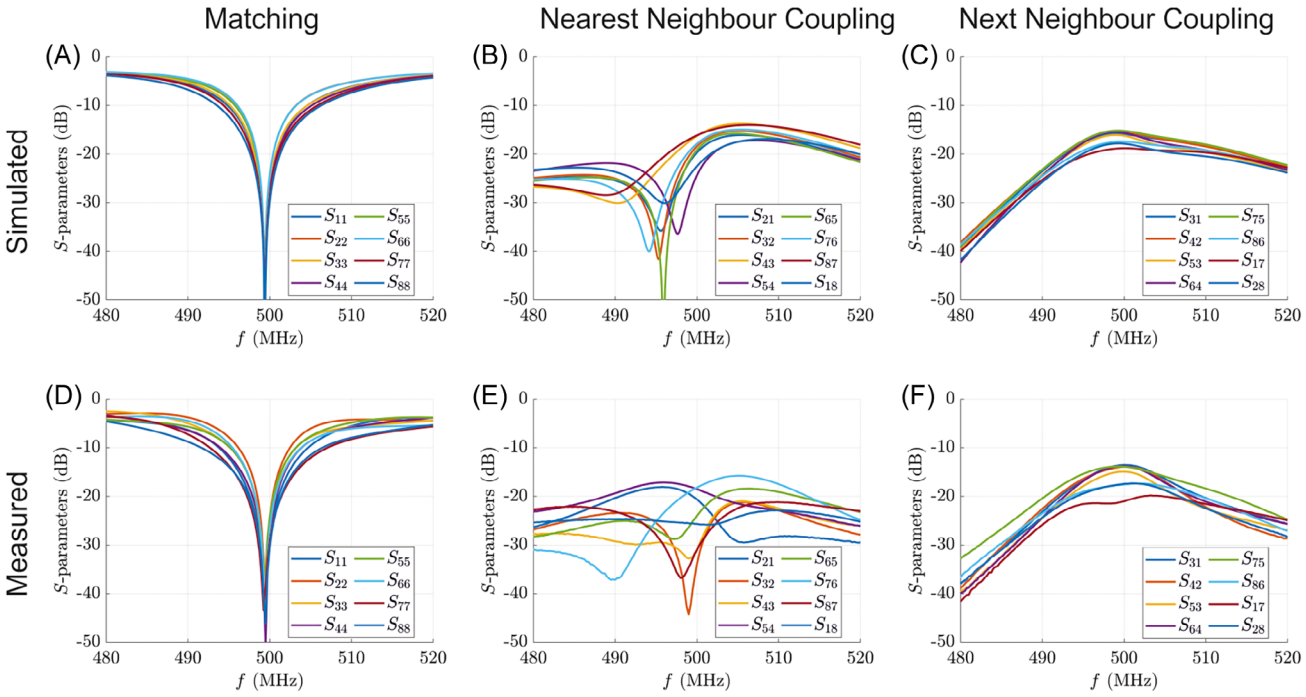

FIGURE 8 (A,B,C) Stimulated and (D,E,F) measured reflection and transmission coefficients of the chosen design when loading with a head and shoulder phantom.

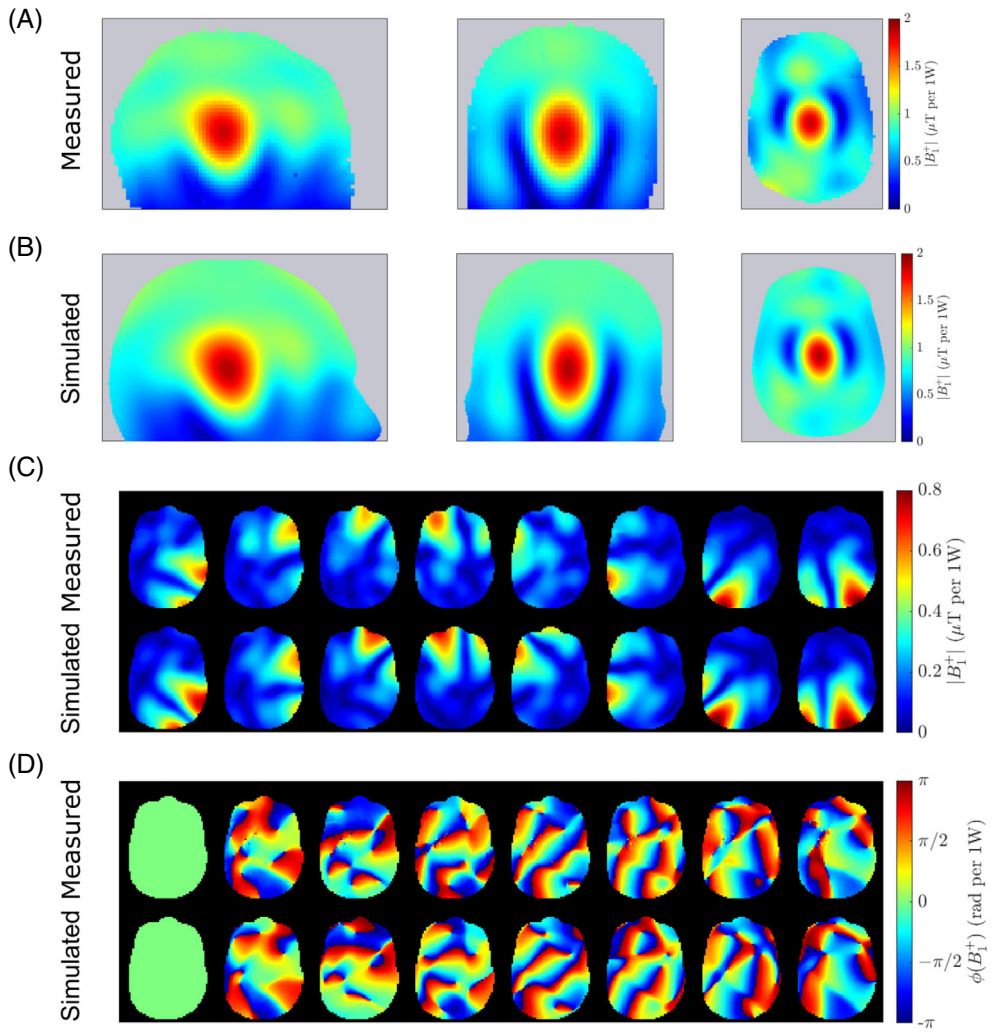

FIGURE 9 (A) Measured and (B) simulated B_1^+ field map in the head and shoulder phantom in circularly polarized mode for 8-W input power. (C) Simulated and measured magnitude and (D) phase maps of the B_1^+ field in the head and shoulder phantom for each individual channel.

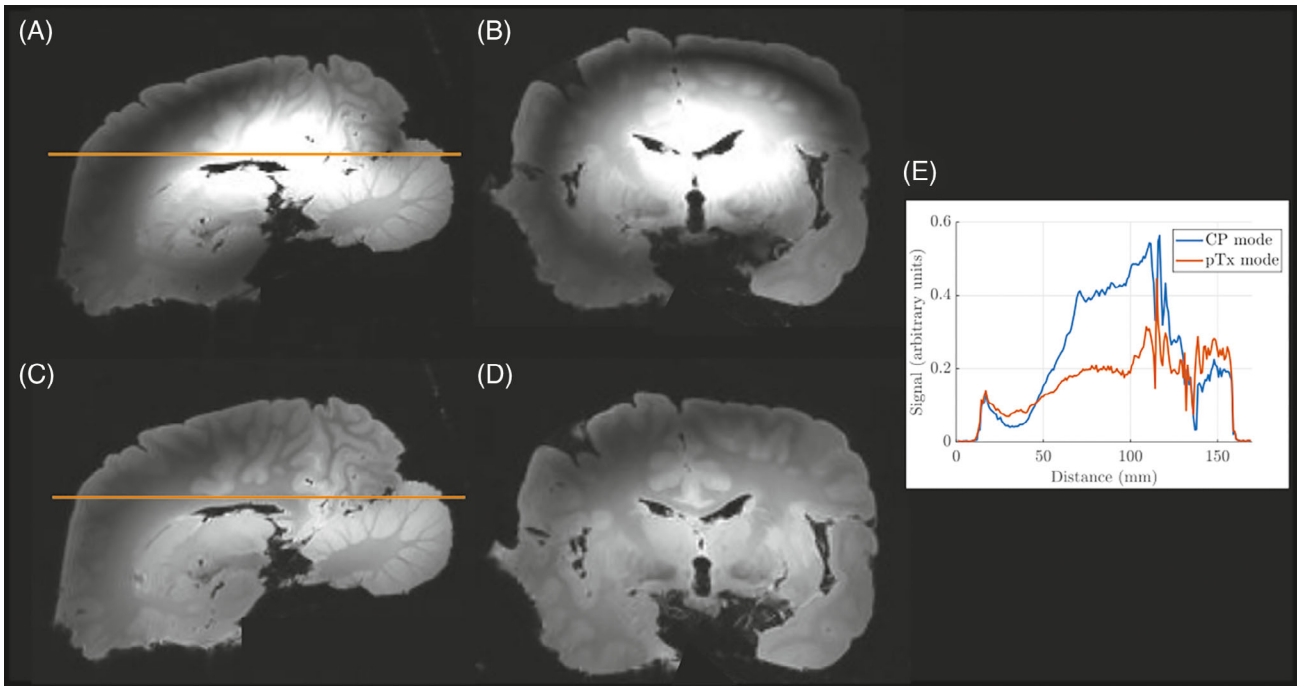

FIGURE 10 Sample (A,C) sagittal and (B,D) coronal slices from the ex vivo data. Images A and B are central sagittal and coronal slices acquired in circularly polarized mode. C and D are corresponding slices in parallel transmit mode with k_T-points design, which mitigates the RF field inhomogeneity problem. (E) Comparison of signal intensity along a horizontal line projection (yellow) highlights the image homogeneity achieved with parallel transmit.

and the measurements yet remain in the periphery of the phantom and are believed to be because of imperfections of the S-matrix in the numerical domain. There is also good agreement in the spatial distribution pattern of the single-channel maps.

Figure 10 presents the ex vivo imaging results. The NRMSE returned from the RF pulse design over the full 3D brain mask was 8.6%. The CP mode of excitation produced an intense, bright spot in the middle of the image as well as a ring of low signal particularly visible in the coronal orientation, because of constructive and deconstructive interferences. The use of parallel transmission here mitigates to a great extent the RF field inhomogeneity problem by flattening the excitation profile and returning a more homogeneous signal intensity image. No bias field correction (e.g., because of receive sensitivity) was performed.

4 | DISCUSSION

This work analyzed the sources of losses to the power applied to a transmit array at 11.7T, and a solution was developed to minimize the losses and maximize the power delivered to the biological tissue. A proof-of-concept transceiver array was constructed to validate the simulation results using phantom and ex vivo scans. Preserving the available RF power is especially important at 11.7T because of the increase in the inherent losses such as on coaxial cables and components. Furthermore, conventional RF shields act as cylindrical waveguides at 11.7T and methods must be developed to alter their dispersion characteristics and minimize power loss because of wave propagation.

We found that folding the ends of the RF shield and subsequent optimization steps reduced the radiated power from 1.47 W in the reference design to 0.19 W in the chosen design. The numerical simulations and experimental validations demonstrate that the folded-end sections increased the cutoff frequency and effectively prevented energy loss because of radiation. As a result, B_1^+ field distribution within the coil is improved as shown in Figure 4D. Further optimization of the coil in conjunction with the RF shield geometry resulted in an improvement of B_1^+ efficiency of up to 42% compared to the reference design.

Duke's full-sized body model and body models truncated at the level of shoulders as well as the neck were evaluated. The radiation loss was the same (0.19 W) for the full-sized and the body model truncated at shoulder level. However, it increased to 0.3 W for the model truncated at the neck level. This allowed us to use the body model truncated at shoulder level in this study. The computation time for the full body model was 32 h and 30 min, whereas the truncated model required 12 h and 30 min, representing a substantial reduction in computation time. The folded end RF shield confines the EM field within the coil volume and hence, the truncated body model was sufficient for numerical studies.

Preliminary simulations showed that the B_1^+ efficiency of an array with a 500-mm RF shield diameter is marginally higher than that of an array with a 400-mm diameter shield. However, this was not included in further optimization because a larger RF coil poses challenges such as inability to align the coil to the isocenter in the XY-plane as well as subject's discomfort in the neck because the coil would sit high on the patient table. Based on the Principle of Reciprocity of MR signals, our result is consistent with Zhang et al.,[47] in which the maximum SNR of receive arrays was shown to monotonically increase with the shield diameter when the loops' axis is perpendicular to the shield side or there is no longitudinal component of the H-field.

Our simulations did not establish a trend between shield length, shield diameter, and radiated power (Figure 7A,B). On all array configurations considered in this work, however, it was observed that the array S-parameters were significantly altered when the folded-end sections were close (less than 4 cm) to the coil elements. Together with the findings in Zhang et al.,[47] our results emphasize the need to optimize RF shield designs in conjunction with the transmit array at UHF to achieve optimal transmit performance.

Our optimization workflow included RFPD simulations to select the optimal configuration, including explicit SAR and power constraints. One weakness of the RFPD simulations was that B_0 field inhomogeneity was not taken into account for simplicity. The 0.5 ms small tip angle pulse, given its short duration, however, should be relatively robust versus B_0 offsets and its performance, therefore, is not much affected. The results demonstrate that the best-performing coil in conventional CP mode, in terms of peak B_1^+ in the center, is not the preferred configuration as per the RFPD simulations. The array with the maximum peak B_1^+ in CP mode indeed does not necessarily imply the preferred configuration for imaging in terms of NRMSE. Given the many degrees of freedom in parallel transmit, the CP mode still was chosen as a simple standard to first guide the optimizations, but one cannot rule out the existence of a more relevant transmit mode. In practice, it also remains useful to have a simple transmit mode for head localization, B_0 and B_1^+ field mapping etc. Our B_1^+ field mapping sequence, for instance here, was an interferometric sequence playing by default the CP mode and where transmit channels were sequentially de-phased by 180° one by one. It is, therefore, desirable that the default-mode yields reasonable field homogeneity to avoid strong B_1^+ voids. For our particular coil architecture, the CP mode returns a relatively smooth profile and close to optimal CV in a static RF shim configuration. Interestingly also, one can observe that the NRMSEs found with RFPD appear to correlate well with the coefficient of variation of the transmit field in CP mode. As a result, this metric could potentially serve as a useful guide and surrogate for RF pulse performance. For the CP mode again, the more homogeneous profile was returned by the $\gamma_{400}(260)$ design with a CV of 26.7%, leading after RFPD of k_T-points to less than 7% and 2% NRMSEs for the small and large flip angle NRMSEs, respectively. The corresponding CV values obtained using volume birdcage coils at 3T and 7T are 13% and 22%, respectively.[48,49] Although $\gamma_{400}(240)$ and $\gamma_{450}(280)$ provided the higher peak B_1^+ values, $\gamma_{400}(260)$ and $\gamma_{450}(240)$ were found to be more suitable for imaging by the RFPD simulations. This suggests in general caution when making design choices based on B_1^+ maps alone, whereby the relationship between optimized NRMSE and field maps is a non-trivial one.

Several transmit arrays for UHF MRI have been proposed, which use different array elements such as loops, dipoles, microstrips, and combinations of loops and dipoles. Although we used a conventional loop array to demonstrate and validate the workflow, design issues that are highlighted in this article will be common for the different array elements at 11.7T. Therefore, the presented workflow is applicable to any of the array types. Future studies will consist of applying this workflow to determine the optimal element type that offers the best performance for MRI at 11.7T.

5 | CONCLUSION

In this paper, we present a new workflow, which is especially beneficial to develop transmit arrays for UHF strengths such as 11.7T. Extensive EM simulations in combination with RFPD simulations were used to identify the suitable array configuration for imaging. An 8-channel transceiver array was fabricated to validate the numerical simulations using phantom and ex-vivo measurements. Analysis of the loss mechanisms and optimizing the RF shield design in conjunction with the array design improved the transmit efficiency by 42% when compared with the reference design. Importantly, the RFPD simulations performed under realistic SAR and power constraints demonstrated that the most suitable array configuration for imaging is not the array that produced the maximum B_1^+ in CP mode, which is contrary to current practice at UHF.

ACKNOWLEDGMENTS

The authors thank Dr. Paul McElhinney (University of Glasgow) for his guidance and support on CST modeling. The authors also thank Dr. Mathieu Santin (Paris Brain Institute-ICM) for providing the ex vivo brain. Brain extraction was approved by the National Biomedicine

Agency (Agence de la Biomédecine) and the French Ministry of Health. This project has received funding from the European Union's Horizon 2020 research and innovation program under grant agreement No. 885876 (AROMA) and from the French government grant managed by the Agence Nationale de la Recherche under the program "Investissements d'avenir" (ANR-21-ESRE-0006).

CONFLICT OF INTEREST STATEMENT

A.M. is an employee of Siemens Healthcare SAS, Saint-Denis, France; and S.G. is a shareholder of MR CoilTech Limited, Glasgow, UK.

ORCID

Son Chu https://orcid.org/0000-0002-4170-777X
Vincent Gras https://orcid.org/0000-0002-4997-2738
Franck Mauconduit https://orcid.org/0000-0002-0128-061X
Nicolas Boulant https://orcid.org/0000-0003-2144-2484
Shajan Gunamony https://orcid.org/0000-0002-3146-6079

REFERENCES

1. Uğurbil K. Imaging at ultrahigh magnetic fields: history, challenges, and solutions. *Neuroimage*. 2018;168:7-32.
2. Budinger TF, Bird MD. MRI and MRS of the human brain at magnetic fields of 14 T to 20 T: technical feasibility, safety, and neuroscience horizons. *Neuroimage*. 2018;168:509-531.
3. Ocali O, Atalar E. Ultimate intrinsic signal-to-noise ratio in MRI. *Magn Reson Med*. 1998;39:462-473.
4. Vaughan JT, Garwood M, Collins C, et al. 7T vs. 4T: RF power, homogeneity, and signal-to-noise comparison in head images. *Magn Reson Med*. 2001;46:24-30.
5. Pohmann R, Speck O, Scheffler K. Signal-to-noise ratio and MR tissue parameters in human brain imaging at 3, 7, and 9.4 tesla using current receive coil arrays. *Magn Reson Med*. 2016;75:801-809.
6. Ladd ME, Bachert P, Meyerspeer M, et al. Pros and cons of ultra-high-field MRI/MRS for human application. *Prog Nucl Magn Reson Spectrosc*. 2018;109:1-50.
7. Cao Z, Park J, Cho ZH, Collins CM. Numerical evaluation of image homogeneity, signal-to-noise ratio, and specific absorption rate for human brain imaging at 1.5, 3, 7, 10.5, and 14T in an 8-channel transmit/receive array. *J Magn Reson Imaging*. 2015;41:1432-1439.
8. Le Ster C, Grant A, Van de Moortele P, et al. Magnetic field strength dependent SNR gain at the center of a spherical phantom and up to 11. 7T. *Magn Reson Med*. 2022;88:2131-2138.
9. US Food & Drug Administration. *FDA Clears First 7T Magnetic Resonance Imaging Device*. US Food & Drug Administration; 2017 [Online]. Available: https://www.fda.gov/news-events/press-announcements/fda-clears-first-7t-magnetic-resonance-imaging-device
10. Medgadget. FDA Clears Most Powerful Clinical MRI. 2020 [Online]. Available: https://www.medgadget.com/2020/11/fda-clears-most-powerful-clinical-mri-scanner.html
11. Vaughan T, DelaBarre L, Snyder C, et al. 9.4 T human MRI: preliminary results. *Magn Reson Med*. 2006;56:1274-1282.
12. Gunamony S, Hoffmann J, Budde J, Adriany G, Ugurbil K, Pohmann R. Design and evaluation of an RF front-end for 9.4 T human MRI. *Magn Reson Med*. 2011;66:594-602.
13. Sadeghi-Tarakameh A, DelaBarre L, Lagore RL, et al. In vivo human head MRI at 10.5 T: a radiofrequency safety study and preliminary imaging results. *Magn Reson Med*. 2020;84:484-496.
14. Quettier L, Aubert G, Belorgey J, et al. Commissioning completion of the iseult whole body 11.7 T MRI system. *IEEE Transact Appl Supercond*. 2020;30:1-5.
15. Allard J, Amadon A, Aubert G, et al. Progress on the commissioning of the Iseult 11.7 T whole-body MRI: first images. in *the 31st Annual Meeting of ISMRM*. London; 2022:Abstract 0382.
16. Chu S, Gras V, McElhinney P, Boulant N, Gunamony S. Design and optimization of transmit arrays for MRI at 11.7T. in *Proceedings of the 31st Annual Meeting of ISMRM*, London 2022:0706.
17. Ounsworth R. *University's Largest Ever Funding Award for UK's most Powerful MRI Scanner*. University of Nottingham; 2022 [Online]. Available: https://blogs.nottingham.ac.uk/researchexchange/2022/06/23/universitys-largest-ever-funding-award-for-uks-most-powerful-mri-scanner/
18. Nowogrodzki A. The world's strongest MRI machines are pushing human imaging to new limits. *Nature*. 2018;563:24-27.
19. Kraff O, Quick HH. 7T: physics, safety, and potential clinical applications. *J Magn Reson Imaging*. 2017;46:1573-1589.
20. Van de Moortele PF, Akgun C, Adriany G, et al. B1 destructive interferences and spatial phase patterns at 7 T with a head transceiver array coil. *Magn Reson Med*. 2005;54:1503-1518.
21. Le Ster C, Mauconduit F, Mirkes C, Vignaud A, Boulant N. Measuring radiofrequency field-induced temperature variations in brain MRI exams with motion compensated MR thermometry and field monitoring. *Magn Reson Med*. 2022;88:1390-1400.
22. Gunamony S, Kozlov M, Hoffmann J, Turner R, Scheffler K, Pohmann R. A 16-channel dual-row transmit array in combination with a 31-element receive array for human brain imaging at 9.4 T. *Magn Reson Med*. 2014;71:870-879.
23. Gunamony S, Mirkes C, Buckenmaier K, Hoffmann J, Pohmann R, Scheffler K. Three-layered radio frequency coil arrangement for sodium MRI of the human brain at 9.4 tesla. *Magn Reson Med*. 2016;75:906-916.
24. Avdievich NI, Giapitzakis I-A, Bause J, Shajan G, Scheffler K, Henning A. Double-row 18-loop transceive-32-loop receive tight-fit array provides for whole-brain coverage, high transmit performance, and SNR improvement near the brain center at 9.4 T. *Magn Reson Med*. 2019;81:3392-3405.
25. Woo M, Delabarre L, Waks M, et al. Comparison of 16-channel asymmetric sleeve antenna and dipole antenna transceiver arrays at 10.5 tesla MRI. *IEEE Trans Med Imaging*. 2020;40:1147-1156.
26. Williams SN, Allwood-Spiers S, McElhinney P, et al. A nested eight-channel transmit array with open-face concept for human brain imaging at 7 tesla. *Front Phys Ther*. 2021;9:1-16.
27. Avdievich NI, Solomakha G, Ruhm L, Bause J, Scheffler K, Henning A. Bent folded-end dipole head array for ultrahigh-field MRI turns "dielectric resonance" from an enemy to a friend. *Magn Reson Med*. 2020;84:3453-3467.
28. Barberi EA, Gati JS, Rutt BK, Menon RS. A transmit-only/receive-only (TORO) RF system for high-field MRI/MRS applications. *Magn Reson Med*. 2000;43:284-289.

29. Wiesinger F, Van de Moortele PF, Adriany G, De Zanche N, Ugurbil K, Pruessmann KP. Potential and feasibility of parallel MRI at high field. *NMR Biomed*. 2006;19:368-378.
30. Uğurbil K, Auerbach E, Moeller S, et al. Brain imaging with improved acceleration and SNR at 7 tesla obtained with 64-channel receive array. *Magn Reson Med*. 2019;82:495-509.
31. Wu X, Tian J, Schmitter S, Vaughan JT, Uğurbil K, Van de Moortele P-F. Distributing coil elements in three dimensions enhances parallel transmission multiband RF performance: a simulation study in the human brain at 7 tesla. *Magn Reson Med*. 2016;75:2464-2472.
32. Kozlov M, Turner R. Fast MRI coil analysis based on 3-D electromagnetic and RF circuit co-simulation. *J Magn Reson*. 2009;200:147-152.
33. Hoffmann J, Shajan G, Scheffler K, Pohmann R. Numerical and experimental evaluation of RF shimming in the human brain at 9.4 T using a dual-row transmit array. *Magn Reson Mater Phys Biol Med*. 2014;27:373-386.
34. Williams SN, McElhinney P, Gunamony S. Ultra-high field MRI: parallel-transmit arrays and RF pulse design. *Phys Med Biol*. 2023;68:1-32.
35. Murphy-Boesch J, Koretsky AP. An in vivo NMR probe circuit for improved sensitivity. *J Magn Reson*. 1969;54:526-532.
36. Christ A, Kainz W, Hahn EG, et al. The virtual family—development of surface-based anatomical models of two adults and two children for dosimetric simulations. *Phys Med Biol*. 2009;55(2):N23-38.
37. Kuehne A, Goluch S, Waxmann P, et al. Power balance and loss mechanism analysis in RF transmit coil arrays. *Magn Reson Med*. 2015;74:1165-1176.
38. Harpen MD. Radiative losses of a birdcage resonator. *Magn Reson Med*. 1993;29:713-716.
39. Kesari V. Metal-and dielectric-loaded waveguide: an artificial material for tailoring the waveguide propagation characteristics. In: Man-Gui H, ed. *University of Electronic Science and Technology of China*. IntechOpen; 2019:1-32.
40. Eichfelder G, Gebhardt M. Local specific absorption rate control for parallel transmission by virtual observation points. *Magn Reson Med*. 2011;66:1468-1476.
41. Le Garrec M, Gras V, Hang M, Ferrand G, Luong M, Boulant N. Probabilistic analysis of the specific absorption rate intersubject variability safety factor in parallel transmission MRI. *Magn Reson Med*. 2017;78:1217-1223.
42. Cloos MA, Boulant N, Luong M, et al. kT-points: short three-dimensional tailored RF pulses for flip-angle homogenization over an extended volume. *Magn Reson Med*. 2012;67:72-80.
43. Hoyos-Idrobo A, Weiss P, Massire A, Amadon A, Boulant N. On variant strategies to solve the magnitude least squares optimization problem in parallel transmission pulse design and under strict SAR and power constraints. *IEEE Trans Med Imaging*. 2013;33:739-748.
44. Gras V, Luong M, Amadon A, Boulant N. Joint design of kT-points trajectories and RF pulses under explicit SAR and power constraints in the large flip angle regime. *J Magn Reson*. 2015;261:181-189.
45. Yarnykh VL. Actual flip-angle imaging in the pulsed steady state: a method for rapid three-dimensional mapping of the transmitted radiofrequency field. *Magn Reson Med*. 2007;57:192-200.
46. Brunner DO, Pruessmann KP. B_1^+ interferometry for the calibration of RF transmitter arrays. *Magn Reson Med*. 2009;61:1480-1488.
47. Zhang B, Adriany G, Delabarre L, et al. Effect of radiofrequency shield diameter on signal-to-noise ratio at ultra-high field MRI. *Magn Reson Med*. 2021;85:3522-3530.
48. Boulant N, Bihan DL, Amadon A. Strongly modulating pulses for counteracting RF inhomogeneity at high fields. *Magn Reson Med*. 2008;60:701-708.
49. Boulant N, Mangin JF, Amadon A. Counteracting radio frequency inhomogeneity in the human brain at 7 tesla using strongly modulating pulses. *Magn Reson Med*. 2009;61:1165-1172.

How to cite this article: Chu S, Gras V, Mauconduit F, Massire A, Boulant N, Gunamony S. Electromagnetic and RF pulse design simulation based optimization of an eight-channel loop array for 11.7T brain imaging. *Magn Reson Med*. 2023;1-14. doi: 10.1002/mrm.29654